39th IAHR WORLD CONGRESS GRANADA, SPAIN 2022 From Snow to Sea 19-24 June 2022

Proceedings of the 39th IAHR World Congress
19–24 June 2022, Granada, Spain
doi://10.3850/IAHR-39WC2521716X20221064

Effects of Geometric Shapes on the Hydrodynamics and Sediment Transport in Lateral Cavities

Luiz Eduardo Domingos de Oliveira[1][2], Johannes Gérson Janzen[1] and Carlo Gualtieri[2]

[1] Federal University of Mato Grosso do Sul, Campo Grande, Brazil,
e-mail luedoliveira@gmail.com, johannesjanzen@gmail.com

[2] University of Napoli Federico II, Napoli, Italy,
e-mail luedoliveira@gmail.com, carlo.gualtieri@unina.it.

Abstract

In riverine systems, lateral cavities are semi-enclosed volumes adjacent to the main channel flowing through its only opened side. These volumes play an important role in the mass transport processes, due to their higher residence time. The shape of the lateral cavity seems to influence the flow structure, although its effect on sediment transport remains unknown. In this study, numerical simulations of the flow past two lateral cavities of distinct shapes were performed to understand the impact of shape in the hydrodynamics and sediment transport. The 3D flow distribution was altered compared to the traditional rectangular shape by losing the secondary circulations near the wall. Moreover, the interface between the main channel and the cavity was a more uniform distribution of velocities in the upstream portion of the cavity with the change in shape. Furthermore, the shape did not influence the general behaviour of sediment transport, however, the peak of variables such as the Rouse and Shields numbers showed a difference of 6% and 135%, respectively.

Keywords: Lateral Cavity; Geometric Shape; Sediment Transport; Large Eddy Simulation (LES); Computational Fluid Dynamics (CFD)

1. INTRODUCTION

In river engineering, an open-channel lateral cavity is a semi-enclosed volume adjacent to the main channel flowing through its opened side. These structures can appear naturally or be constructed and be either a single cavity (as in the present study), a cavity between groynes or a series of cavities. The importance of lateral cavities relies on four main characteristics: (1) to increase lateral macro-roughness in rivers (Juez *et al.*, 2018), (2) to drive mass exchange processes with the open channel (Gualtieri, 2008, 2010; Jackson *et al.*, 2015; Mignot *et al.*, 2016; Ouro *et al*., 2020), (3) to act as transient storage zones (Jackson *et al.*, 2013; Drost *et al.*, 2014; Jackson *et al.*, 2015), and (4) to enhance biodiversity in the system (Watts and Johnson, 2004; Ribi *et al.*, 2014; Harvey, 2016). The common link between these characteristics is the slow velocity flow that occurs inside of this structure, for instance, in cavities between groynes, the velocity magnitude can be down to 25 % of the main channel (region of unaltered flow) velocity (Sukhodolov, 2014). This difference in magnitude forms a mixing layer between the main channel and the cavity. This region is characterised by a gradient of velocities and is responsible for the transport of vortexes and mass between the zones. Understanding the variables that alter the three-dimensional (3D) flow dynamics would allow a better cavity design to accomplish one or several of these goals.

The flow past one or more square or rectangular lateral cavities has been well studied for both hydrodynamics and mass exchange. Previous studies have determined that mass exchange and the flow are influenced by geometrical parameters, such as the aspect ratio between width and length that determine the flow patterns inside of the cavity (Jackson *et al.*, 2012, 2013; Mignot *et al.*, 2019) and cavity depth (McCoy *et al.*, 2007, 2008; Jackson *et al.*, 2013). Although the shape of the cavity can also alter the flow structure (Ozalp *et al.*, 2010; Jackson *et al.*, 2013), however, these studies did not assess how the changes in the flow would impact mass transport and despite its importance, this influence remains unknown, especially in less idealised geometries such as trapezoids. In this study, a numerical model was developed to investigate the effect of shape in the hydrodynamic and sediment transport in lateral cavities.

This paper is organized into four main sections. Following the introduction, the details of the numerical model were described, along with the grid independence test and solution quality. Third, the main results about flow hydrodynamics, mass exchange and sediment transport were presented and finally, conclusive remarks about the influence of geometrical shape in a single circulation lateral cavity were presented.

2. NUMERICAL MODEL

2.1 Model Equations

The simulations were performed in a Computational Fluid Dynamics (CFD) environment. The approach used to solve the flow and turbulence was the Large Eddy Simulation (LES), which uses spatial filtering of the Navier-Stokes equations (Rodi *et al.*, 2013). In this model the fluid was considered incompressible, which simplifies the conservation equations of mass and momentum into:

$$\frac{\partial \overline{u_i}}{\partial x_i} = 0 \quad [1]$$

$$\frac{\partial \overline{u_i}}{\partial t} + \frac{\partial}{\partial x_j}\left(\overline{u_i}\overline{u_j}\right) = \frac{-1}{\rho}\frac{\partial \overline{p}}{\partial x_i} + \frac{\partial}{\partial x_j}\left[\vartheta\left(2\bar{S}_{ij}\right) - \tau_{ij}\right] \quad [2]$$

in which the overbar indicates resolved quantities, and i and j = 1, 2, 3 correspond to x, y, z directions, respectively; u_i (m/s) is the velocity component in the i direction, ρ (kg/m³) is the fluid density, p (N/m²) is the dynamic pressure, ϑ (m²/s) is the kinematic viscosity, S_{ij} (1/s) is the strain-rate tensor and τ_{ij} (m²/s²) is the subgrid-scale stress. S_{ij} and τ_{ij} are given by:

$$\bar{S}_{ij} = \frac{1}{2}\left(\frac{\partial u_i}{\partial x_j} + \frac{\partial u_j}{\partial x_i}\right) \quad [3]$$

$$\tau_{ij} = \overline{u}_i\overline{u}_j - \overline{u_i u_j} \quad [4]$$

τ_{ij} represents the effect of unresolved small-scale motion on the resolved flow, and is based on the eddy-viscosity assumption:

$$\tau_{ij} - \frac{1}{3}\tau_{kk}\delta_{ij} = -\vartheta_t\left(2\bar{S}_{ij}\right) \quad [5]$$

where ϑ_t (m²/s) is the eddy viscosity. The Wall-Adapting Local Eddy-viscosity (WALE) model, proposed by Nicoud and Ducros (1999), was chosen as the subgrid-scale model to calculate ϑ_t.

2.2 Numerical Model and Boundary Conditions

The simulations were calculated with the open-source package OpenFOAM (version 1912), in which the module pimpleFOAM was chosen to discretize the governing equations and numerical schemes. This module employs the finite volume method (FVM) in a transient formulation. To solve the convection-diffusion equations, the implicit second-order backward time-stepping scheme and additional second-order schemes were used. The residual tolerance was set to 1E-04 for pressure and 1E-06 for other variables. The time increment was set as adaptative with a maximum Courant number of 0.9 and a maximum time-step of 0.05s. The average time-step size was 0.003s. The simulation ran for nearly *150 H/U* to stabilize the solution and develop the flow, after this period the time-averaging procedure started and continued for more *200 H/U* to ensure that the averaged values were static.

The 3D geometry consisted of a lateral cavity adjacent to a rectangular open channel. The main channel was the same for both lateral cavity shapes (rectangular and trapezoidal). The main channel and rectangular lateral cavity geometries and flow conditions were extracted from Xiang et al. (2019), in order to validate our proposed model. The main channel was $L = 1.25m$ long, $B = 0.30m$ wide and had a depth $H = 0.10m$ that is held constant throughout all the geometry. The first simulation had a lateral cavity with a rectangular shape (Figure 1 a), this cavity was $W = 0.15m$ wide and $L = 0.25m$ long and had a volume of $V = 3.75E\text{-}3\ m^3$, resulting in the aspect ratio $W/L = 0.6$, which corresponds to a one-gyre system to be formed inside the cavity (Mignot *et al.*, 2019). The second simulation had a lateral cavity with a trapezoidal shape (Figure 1 b) that was calculated to have the same aspect ratio W/L and volume, this cavity was $W \approx 0.197m$ wide, a smaller length of $L_1 \approx 0.052m$ and bigger of $L_2 \approx 0.328m$ long. In all cases, the flow in the main channel was turbulent ($Re = 9000$) and subcritical ($Fr = 0.102$), with an averaged velocity $U = 0.101\ m/s$.

The boundary conditions remained the same for both simulations. The rigid-lid approximation was applied at the free surface of the domain ($z = 0.10m$), which is valid for subcritical flows within $Fr < 0.36$ (Khosronejad

et al., 2020). The longitudinal XZ plane, located at $y = 0m$, where the main channel was restricted in the domain, was defined as a free-slip wall. The width of the main channel covered by the numerical model was only 0.30 m (the full width of the experimental main channel was 0.85 m) to avoid having to resolve the boundary layer near the opposite channel wall and save grid points. At this location, the effect caused by the cavity is negligible (Brevis *et al.*, 2014) and the flow is parallel and nearly uniform so that a free-slip condition was applied. The inlet portion of the domain ($x = 0m$) was calculated in two phases: (a) precalculated velocity fields that were fully developed in a periodic channel, under the same flow conditions and the main channel geometry and (b) the resulting fields (Reynolds stresses, velocity and turbulence intensity) were interpolated into the boundary condition turbulence Divergence-Free Synthetic Eddy Method (turbulentDF-SEM) that used these predeveloped fields to synthesize eddies into the domain (Poletto *et al.*, 2013). A convective outflow boundary condition was adopted at the outlet ($x = 1.25m$), in which the zero-gradient condition allows the flow to exit the domain without having any backflow. The bottom of the domain ($z = 0m$), and the walls of the main channel ($y = 0.30m$) and the cavity were considered as no-slip walls. The turbulent viscosity was modelled in all the no-slip walls of the domain with the Spalding wall function, where all parameters were left as default.

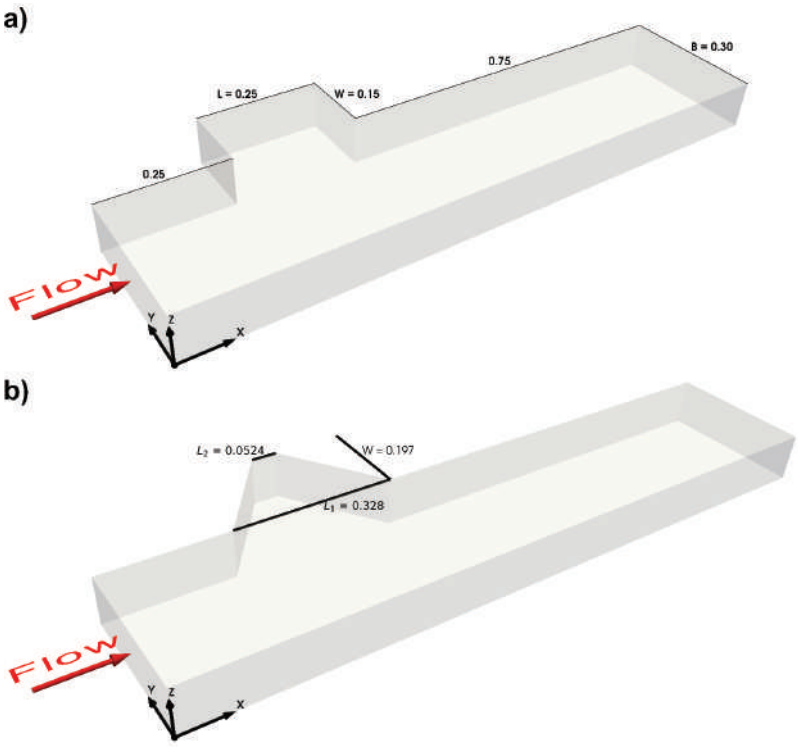

Figure 1. Computational domain with coordinates, dimensions, and the main boundary conditions. a) rectangular cavity and b) trapezoidal cavity. All dimensions are in meters.

Both domains received the same meshing parameters. The computational points in the entire domain were displaced in a rectangular mesh. The main channel was divided into a mesh of 120X120X40, for the streamwise (*x-axis*), spanwise (*y-axis*) and vertical directions (*z-axis*); respectively, while the cavity was divided in 80X80X40. Figure 2 a shows the computational mesh in the free-surface plane, Figure 2 b shows the increase in cells density around the interface between the lateral cavity and the main channel and Figure 2c shows the distribution of cells in the vertical direction for all locations of the domain. The total number of hexahedral elements was 1.408.000 elements and a maximum $y^+ = 6.8$ and $z^+ = 2.2$. The discretization of the domain was defined with the mesh uncertainty evaluation proposed by Dutta and Xing (2018). Three meshes were employed: a coarse grid with 639,680 elements, a medium grid with 1,408,000 elements, and a fine mesh with 3,132,800 elements, where the refinement rate between the meshes was 1.40. The calculated uncertainty was 1.74% in the medium mesh, which was chosen to continue. The meshes were decomposed and solved on 14 cores each (AMD Opteron 6376 with clock frequencies of 2.3 GHz) and took ≈ 54 hours to simulate 100 s of flow.

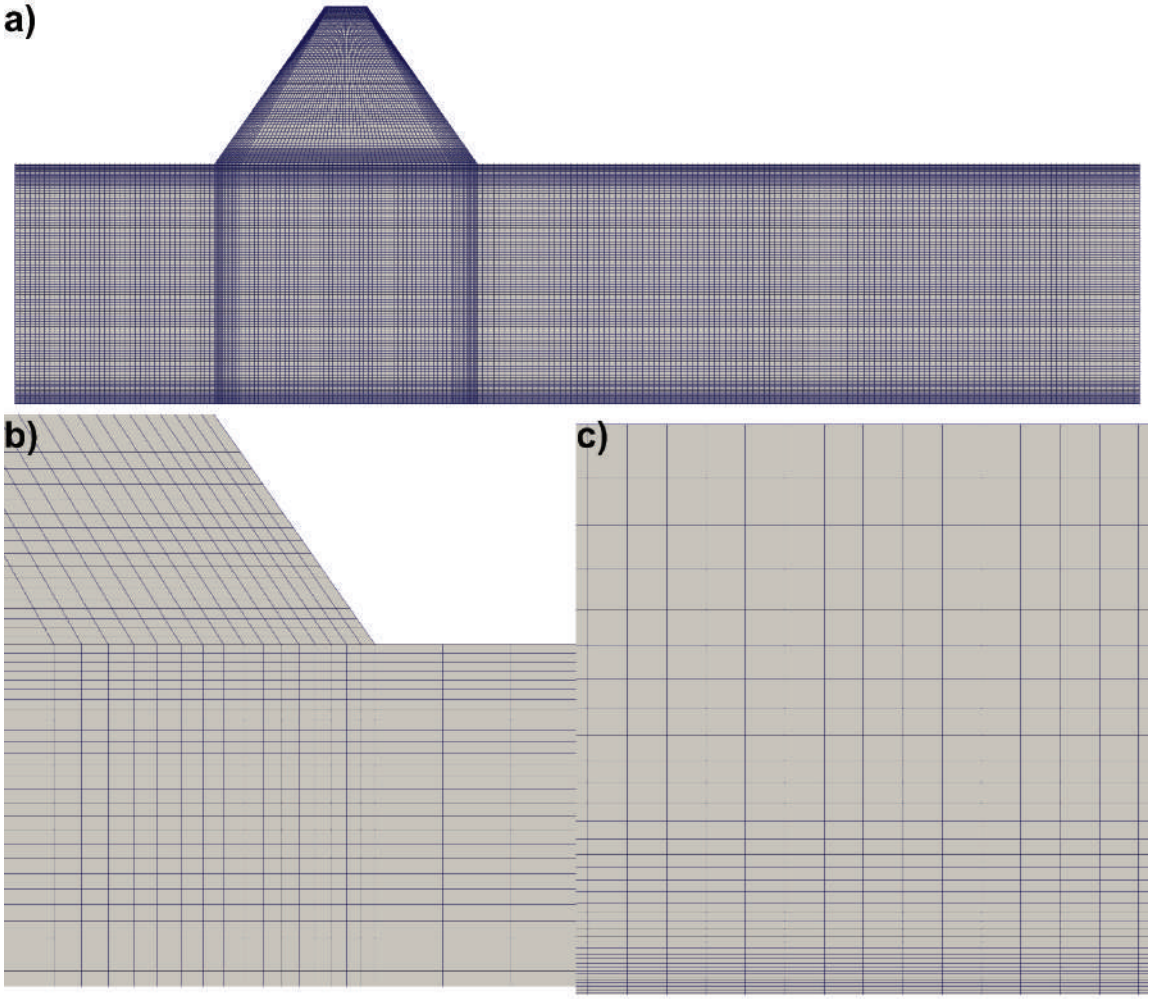

Figure 2. Computational mesh in the trapezoidal case a) mesh in the free surface plane, b) mesh near the interface between the lateral cavity and the main channel and c) mesh in a vertical plane.

3. RESULTS

3.1 Hydrodynamics and Mass Exchange

Figure 3 shows the 2D time-averaged velocity at different depths of the flow and its streamlines. In both cavities, the flow developed from a quasi-circular shape into an ellipsoidal, for the rectangular cavity, and an oval shape for the trapezoidal cavity. At any depth of the flow, some small circulations near the corners of the geometry are expected in simplified geometries, which can be seen in the right column of Figure 3. Although, this behaviour did not occur for the trapezoidal shape, similar to the triangular and semi-circular shape from Ozalp et al. (2010). The lower angle between the walls likely promotes a more uniform flow distribution in the proximity of the corners, which maintains the flow with a single circulation cell instead of breaking into separated vortexes. To some extent, this means that the mass is better spread inside the cavity volume and no secondary circulations of slow velocity appears, which can potentially reduce the mean residence time of mass (Engelhardt *et al.*, 2004; McCoy *et al.*, 2007, 2008; Jackson *et al.*, 2012).

The mixing layer remained unchanged in both shapes, in the XY plane. The flow still enters from the most downstream (right portion) part of the cavity and exits through the upstream (left portion) (Figure 3 and Figure 4) [similar to Akutina (2015) and Engelen *et al.* (2021)]. Albeit the change in shape reduced the extent of the zones with a velocity close to zero in the trapezoidal cavity ($0 < x/L \lesssim 0.62$) compared to the rectangular shape ($0.08 \lesssim x/L \lesssim 0.62$), even though, the velocity magnitudes remained the same in both the shapes. Interestingly, the extent of the zone with negative velocities near the downstream ($x/L \approx 1$) increased in the trapezoidal cavity, which indicates that possibly this shape allows the development of larger vortexes along the mixing layer.

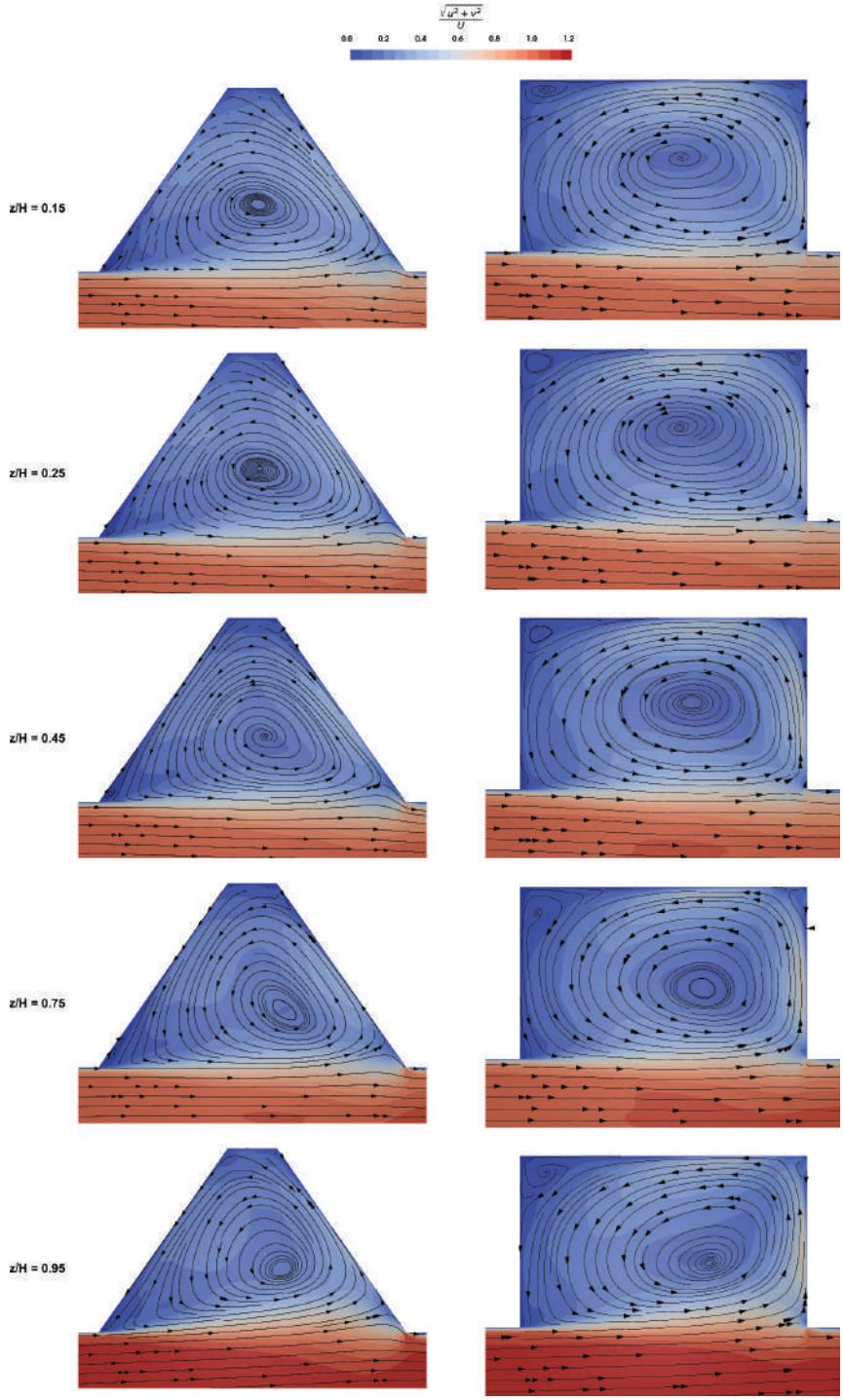

Figure 3. Time-averaged horizontal velocity field (contour plot and streamlines) at different elevations (z/H).

The mass exchange between the main channel and the lateral cavity was investigated with an inert tracer. After the flow was developed at t = 150 H/U the entire volume of the lateral cavity was filled with tracer, following the procedure of Sandoval *et al.* (2019). The tracer concentration was spatially averaged at the cavity volume in all time-steps. The results from the simulation were then fitted into a first-order decay curve (Eq. 6).

$$C(t) = C_0 \exp(-t/T) \quad [6]$$

where C_0 = 1 is the initial concentration, t (s) is the experiment time and T (s) is the adjusted mean residence time. The values of T were adjusted using the Least-Squares method.

Figure 5 shows the concentration decay inside both shapes. The trapezoidal shape has a ≈24% faster mass decay compared to the rectangular shape. This difference was larger than the estimated ≈6% from the model from Eq. 7 extracted from Jackson *et al.* (2013). The effect of the velocity fields was not considered in the mentioned model, which is probably the source of these differences since the lack of the secondary gyres in the corners of the geometry reduces the amount of tracer trapped in a zone with velocities close to zero and it is likely to increase the rate of advection of the tracer cloud within this region.

$$\frac{TU}{L} = 28\left(\frac{Ud_E}{\nu}\right)^{0.15}\left(\frac{U}{\sqrt{gd_E}}\right)^{0.56}\left(\frac{W^{1.5}d_c^{1.5}}{L^2 d_E}\right)^{0.44} - 5 \qquad [7]$$

where d_E = H (m) is the average depth of the shear layer, v is the kinematic viscosity, g (m/s^2) gravitational acceleration and d_c = H (m) is the averaged depth inside the cavity.

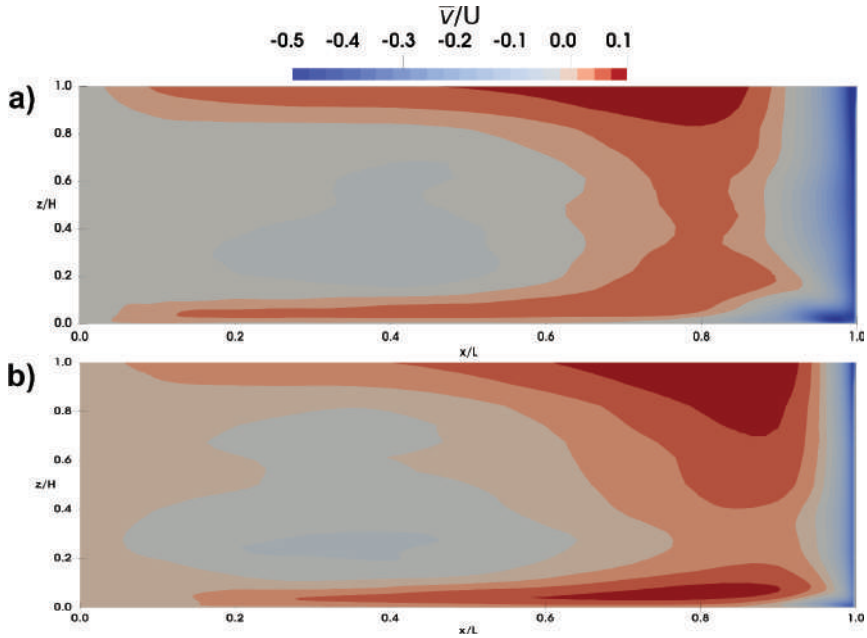

Figure 4. The time-averaged y-velocity field at the interface between the main channel and the lateral cavity: a) trapezoidal and b) rectangular. Positive values indicate a flow towards the cavity whilst negative towards the main channel.

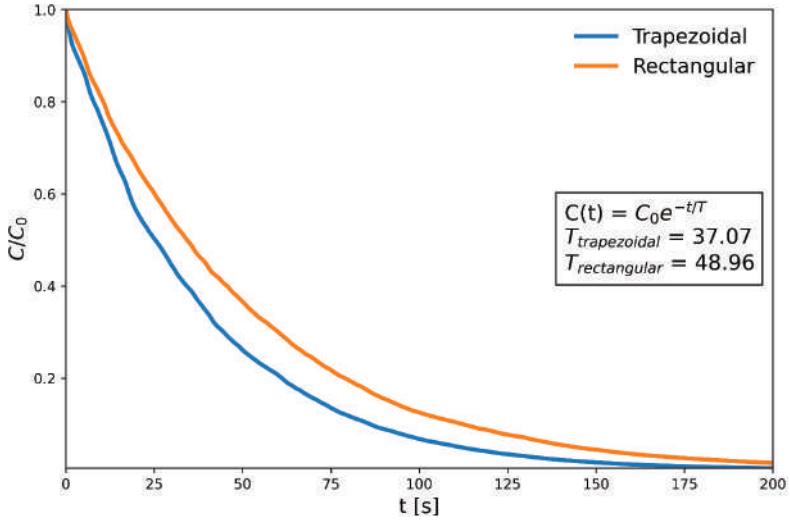

Figure 5. Spatially averaged decay of tracer concentration inside of the lateral cavity volume and the adjusted values of T (s), the mean residence time.

3.2 Sediment Transport

In this section, we present and discuss the results regarding the resistance to sediment movement [Shields number (Eq. 9)] and the type of sediment transport [Rouse Number (Eq. 8)]. We conducted tests for all ranges of sands, in which typical values of particle diameter and settling velocity (Table 1) were extracted from Table 5.4 in Julien (2010).

$$\mathrm{R_o} = \frac{w_s}{\kappa u_*} \quad [8]$$

$$\mathrm{S_h} = \frac{\rho u_*}{(\rho_s - \rho) g d_p} \quad [9]$$

$$\mathrm{u_*} = \sqrt{\tau_b / \rho} \quad [10]$$

where, w_s (m/s) is the particle settling velocity, $\kappa = 0.41$ is the von Karmán constant, u_* (m/s) is the shear velocity (Eq. 10), ρ (kg/m^3) is the specific mass of water, $\rho_s = 2650$ (kg/m^3) is the specific mass of sediment (typical value for quartz and clay minerals), d_p (m) particle diameter and τ_b (kg/ms^2) is the bed shear stress.

Table 1. Typical values of particle diameter (d_p), settling velocity (w_s) extracted from Table 5.4 in Julien (2010).

Sand Granulometry	d_p [m]	w_s [m/s]
Very Fine	0.0000625	0.112
Fine	0.000125	0.0703
Medium	0.00025	0.036
Coarse	0.0005	0.0128
Very Coarse	0.001	0.00347

Table 2. Estimated results of Rouse number (Ro) and Shields number (Sh) inside the lateral cavity at z = 20 d_p. Values on the left of the bar indicate the trapezoidal shape and, on the right, the rectangular shape. The mean values represent a spatial averaging of the values in the XY plane.

Sediment	Rouse Number				Shields Number			
	Min	Max	Mean	Median	Min	Max	Mean (10^{-2})	Median (10^{-2})
Very Fine	0 / 0	96.91 / 353.96	3.75 / 4.32	2.71 / 2.85	0 / 0	0.42 / 0.16	2.85 / 1.76	0.87 / 0.76
Fine	0 / 0	817.23 / 1326.59	10.26 / 10.37	6.90 / 7.10	0 / 0	0.25 / 0.12	2.30 / 1.49	0.89 / 0.83
Medium	0 / 0	727.58 / 820.02	23.37 / 23.82	15.49 / 16.89	0 / 0	0.15 / 0.07	1.65 / 1.13	0.69 / 0.57
Coarse	0 / 0	1391.59 / 3688.25	43.12 / 45.63	29.95 / 32.62	0 / 0	0.12 / 0.03	0.97 / 0.61	0.38 / 0.29
Very Coarse	0 / 0	7438.42 / 3759.89	75.57 / 80.01	53.33 / 57.89	0 / 0	0.04 / 0.01	0.45 / 0.24	0.15 / 0.12

Table 2 summarises the statistical values of the Rouse number (Ro) and Shields number (Sh) inside the cavity at $z = 20d_p$. In both shapes, the mean and median values were always within the same class of movement $Ro > 2.5$, bedload transport. In terms of distribution, Ro maintained constant for the diameters above medium through all the XY plane and was dependent on the flow only for fine and very fine sands (Figure 6). It seems that in terms of sediment transport type the mixing layer has a larger effect on trapezoidal forms, as the distribution of values below 2.5 was spatially larger than in the rectangular shape. This is related to the way that the stream hits the downstream wall at low depths (Figure 3), in rectangular shapes the circulation inside the cavity has lines quasi-parallel to the flow near the mixing layer, while in trapezoidal shapes there is an inclination towards the cavity. Although, there was not a large difference, ≈2%, in the averaged values of Ro in fine and very fine granulometries. The maximum value of all tests was Sh = 0.42 (trapezoidal) and Sh = 0.16 (rectangular), at the downstream wall that receives the first jet, while the interior of the cavity was close to 0, which explains the low average in Table 2. This is a result of a small magnitude of shear stress inside the cavity (averaged at the order of τ ≈ 1E-03 kg/ms) and that the values of shear stress inside the trapezoidal shape was approximately the double of those in the rectangular cavity.

The sediment motion was also analysed with two known curves: Hjulström and Shields curve (Figure 7). Figure 7 a) shows that in the zones with the maximum and minimum velocity (region at the downstream wall of the cavity, see Figure 4) sediment transport can occur, while the spatially averaged behaviour of sediment is the deposition, which the rectangular shape still presents the farthest values from the limit, possibly due to the presence of the secondary circulations. This connects to one of the main characteristics of the lateral cavity, the entrapment of sediments, that remained unaltered with the change of shape. Although, with the Shields curve in Figure 7 b) the granulometry above medium was on average under the movement zone. Furthermore, the difference in behaviour remained the same with the rectangular cavity tending to smaller values of shear stress than the trapezoidal shape. In the shields diagram, there was a change in sediment status depending on the shape for both maximum and spatially averaged values, although not for the median, which is at least half of the averaged values (Table 2). The difference between the median and averaged values remained similar in both shapes.

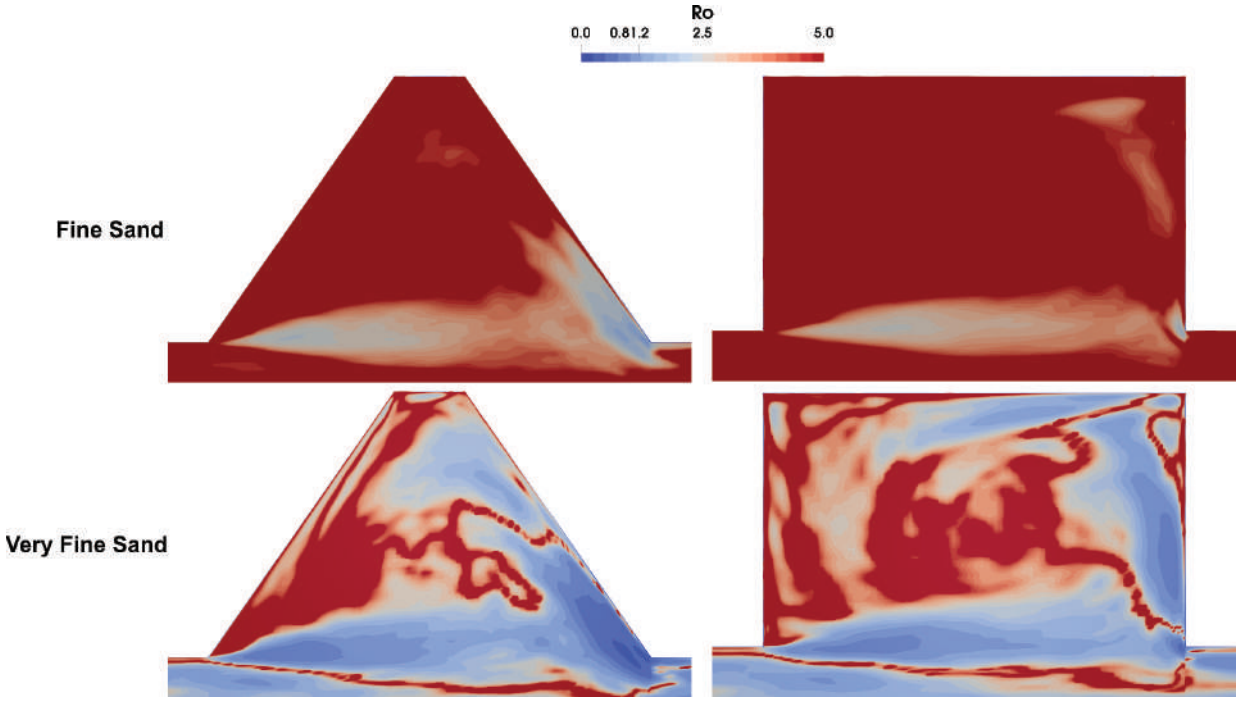

Figure 6. Contours of the Rouse number in the cavity at the depth z = 20d_p, the first row represents the values for fine sand and the second for very fine sand.

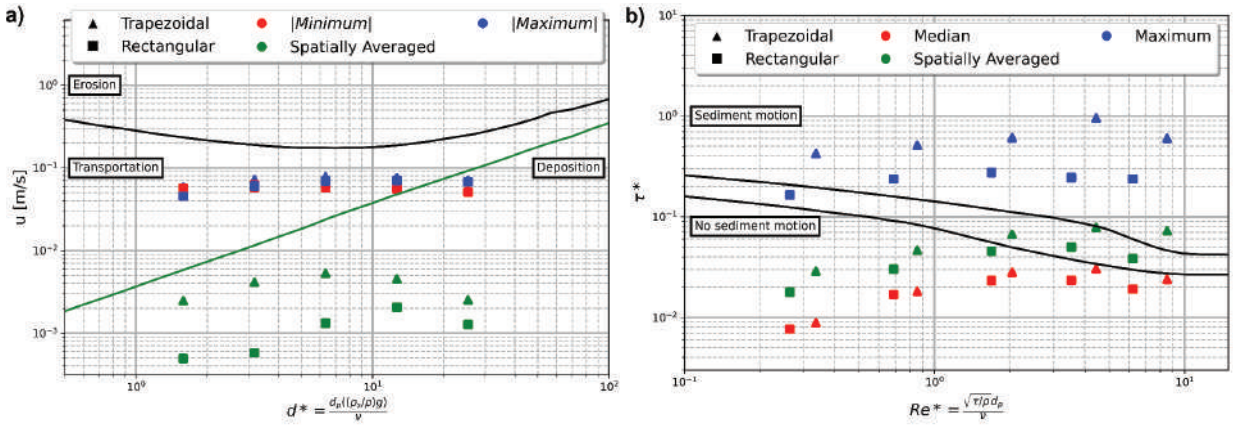

Figure 7. a) Hjulström diagram and b) Shields diagram

4. CONCLUSIONS

This study investigated the influence of shape in hydrodynamics, mass exchange and sediment transport in lateral cavities. The trapezoidal shape could suppress secondary circulations at the corners of the cavity, found in the rectangular shape, which can indicate a mixing without dead corners inside the cavity. This was

further explored with the addition of tracers that proved that the trapezoidal shape has a smaller mean residence time and thus a faster exchange rate between the main channel and the lateral cavity. Furthermore, the distribution of the transversal velocity across the interface, between the main channel and the lateral cavity, was smoother at the upstream of the cavity in the trapezoidal shape. In terms of sediment transport, the expected type of transport is only affected by the flow for fine and very fine granulometries of sand, whereas the effect of the mixing layers seemed larger in the trapezoidal shape. Moreover, the change is sediment motion status could be identified with the change of shape, for both the spatially averaged and maximum values in the Shields diagram, which may be related to the changes promoted in the mixing layer, topic that must be explored in the future.

5. ACKNOWLEDGEMENTS

The present study was carried out under the financial supports from the Coordenação de Aperfeiçoamento de Pessoal de Nível Superior – Brazil (CAPES) – Finance Code 001, CAPES - Institutional Internationalization Program (Print) and the computational time granted at Lobo Carneiro cluster located in NACAD/Coppe - Rio de Janeiro, Brazil.

6. REFERENCES

Akutina, Y. (2015) *Experimental investigation of flow structures in a shallow embayment using 3D-PTV*. McGill University. Available at: https://escholarship.mcgill.ca/concern/theses/pz50gz965.

Brevis, W., García-Villalba, M. and Niño, Y. (2014) 'Experimental and large eddy simulation study of the flow developed by a sequence of lateral obstacles', *Environmental Fluid Mechanics*, 14(4), pp. 873–893. doi: 10.1007/s10652-013-9328-x.

Drost, K. J., Apte, S. R., Haggerty, R. and Jackson, T. (2014) 'Parameterization of Mean Residence Times in Idealized Rectangular Dead Zones Representative of Natural Streams', *Journal of Hydraulic Engineering*, 140(8), p. 04014035. doi: 10.1061/(asce)hy.1943-7900.0000879.

Dutta, R. and Xing, T. (2018) 'Five-equation and robust three-equation methods for solution verification of large eddy simulation', *Journal of Hydrodynamics*, 30(1), pp. 23–33. doi: 10.1007/s42241-018-0002-0.

Engelen, L., Perrot-Minot, C., Mignot, E., Rivière, N. and De Mulder, T. (2021) 'Lagrangian study of the particle transport past a lateral, open-channel cavity', *Physics of Fluids*, 33(1). doi: 10.1063/5.0030922.

Engelhardt, C., Krüger, A., Sukhodolov, A. and Nicklisch, A. (2004) 'A study of phytoplankton spatial distributions, flow structure and characteristics of mixing in a river reach with groynes', *Journal of Plankton Research*, 26(11), pp. 1351–1366. doi: 10.1093/plankt/fbh125.

Gualtieri, C. (2008) 'Numerical simulation of flow patterns and mass exchange processes in dead zones', *Proc. iEMSs 4th Biennial Meeting - Int. Congress on Environmental Modelling and Software: Integrating Sciences and Information Technology for Environmental Assessment and Decision Making, iEMSs 2008*, 1, pp. 150–161.

Gualtieri, C. (2010) 'Numerical simulation of mass exchange processes in a dead zone of a river', in *Advances in Environmental Fluid Mechanics*. Singapore: World Scientific, pp. 249–274. doi: 10.1142/9789814293006_0012.

Harvey, J. W. (2016) 'Hydrologic Exchange Flows and Their Ecological Consequences in River Corridors', in Jones, J. B. and Stanley, E. H. (eds) *Stream Ecosystems in a Changing Environment*. Boston: Academic Press, pp. 1–83. doi: 10.1016/B978-0-12-405890-3.00001-4.

Jackson, T. R., Haggerty, R., Apte, S. V., Coleman, A. and Drost, K. J. (2012) 'Defining and measuring the mean residence time of lateral surface transient storage zones in small streams', *Water Resources Research*, 48(10), pp. 1–20. doi: 10.1029/2012WR012096.

Jackson, T. R., Haggerty, R., Apte, S. V. and O'Connor, B.L. (2013) 'A mean residence time relationship for lateral cavities in gravel-bed rivers and streams: Incorporating streambed roughness and cavity shape', *Water Resources Research*, 49(6), pp. 3642–3650. doi: 10.1002/wrcr.20272.

Jackson, T. R., Haggerty, R., Apte, S. V. and Budwig, R. (2015) 'Flow structure and mean residence times of lateral cavities in open channel flows: influence of bed roughness and shape', *Environmental Fluid Mechanics*, 15(5), pp. 1069–1100. doi: 10.1007/s10652-015-9407-2.

Jackson, T. R., Haggerty, R. and Apte, S. V. (2013) 'A fluid-mechanics based classification scheme for surface transient storage in riverine environments: Quantitatively separating surface from hyporheic transient storage', *Hydrology and Earth System Sciences*, 17(7), pp. 2747–2779. doi: 10.5194/hess-17-2747-2013.

Juez, C., Bühlmann, I., Maechler, G., Schleiss, A.J. and Franca, M.J. (2018) 'Transport of suspended sediments under the influence of bank macro-roughness', *Earth Surface Processes and Landforms*, 43(1), pp. 271–284. doi: 10.1002/esp.4243.

Julien, P. Y. (2010) *Erosion and Sedimentation*. 2nd edn, *Eos, Transactions American Geophysical Union*.

2nd edn. Cambridge: Cambridge University Press. doi: 10.1017/CBO9780511806049.
Khosronejad, A., Arabi, M. G., Angelidis, D., Bagherizadeh, E., Flora, K. and Farhadzadeh, A. (2020) 'A comparative study of rigid-lid and level-set methods for LES of open-channel flows: morphodynamics', *Environmental Fluid Mechanics*, 20(1), pp. 145–164. doi: 10.1007/s10652-019-09703-y.
McCoy, A., Constantinescu, G. and Weber, L. (2007) 'A numerical investigation of coherent structures and mass exchange processes in channel flow with two lateral submerged groynes', *Water Resources Research*, 43(5), pp. 1–26. doi: 10.1029/2006WR005267.
McCoy, A., Constantinescu, G. and Weber, L. J. (2008) 'Numerical Investigation of Flow Hydrodynamics in a Channel with a Series of Groynes', *Journal of Hydraulic Engineering*, 134(2), pp. 157–172. doi: 10.1061/(ASCE)0733-9429(2008)134:2(157).
Mignot, E., Cai, W., Launay, G., Riviere, N. and Escauriaza, C. (2016) 'Coherent turbulent structures at the mixing-interface of a square open-channel lateral cavity', *Physics of Fluids*, 28(4). doi: 10.1063/1.4945264.
Mignot, E., Cai, W. and Riviere, N. (2019) 'Analysis of the transitions between flow patterns in open-channel lateral cavities with increasing aspect ratio', *Environmental Fluid Mechanics*, 19(1), pp. 231–253. doi: 10.1007/s10652-018-9620-x.
Nicoud, F. and Ducros, F. (1999) 'Subgrid-scale stress modelling based on the square of the velocity gradient tensor', *Flow, Turbulence and Combustion*, 62(3), pp. 183–200. doi: 10.1023/A:1009995426001.
Ouro, P., Juez, C. and Franca, M. (2020) 'Drivers for mass and momentum exchange between the main channel and river bank lateral cavities', *Advances in Water Resources*, 137. doi: 10.1016/j.advwatres.2020.103511.
Ozalp, C., Pinarbasi, A. and Sahin, B. (2010) 'Experimental measurement of flow past cavities of different shapes', *Experimental Thermal and Fluid Science*, 34(5), pp. 505–515. doi: 10.1016/j.expthermflusci.2009.11.003.
Poletto, R., Craft, T. and Revell, A. (2013) 'A new divergence free synthetic eddy method for the reproduction of inlet flow conditions for les', *Flow, Turbulence and Combustion*, 91(3), pp. 519–539. doi: 10.1007/s10494-013-9488-2.
Ribi, J. M., Boillat, J. L., Peter, A. and Schleiss, A. J. (2014) 'Attractiveness of a lateral shelter in a channel as a refuge for juvenile brown trout during hydropeaking', *Aquatic Sciences*, 76(4), pp. 527–541. doi: 10.1007/s00027-014-0351-x.
Rodi, W., Constantinescu, G. and Stoesser, T. (2013) *Large-Eddy Simulation in Hydraulics*. 1st edn. Edited by P. A. Davies. Leiden: CRC Press/Balkema.
Sandoval, J., Mignot, E., Mao, L., Pastén, P., Bolster, D. and Escauriaza, C. (2019) 'Field and Numerical Investigation of Transport Mechanisms in a Surface Storage Zone', *Journal of Geophysical Research: Earth Surface*, 124(4), pp. 938–959. doi: 10.1029/2018JF004716.
Sukhodolov, A. N. (2014) 'Hydrodynamics of groyne fields in a straight river reach: Insight from field experiments', *Journal of Hydraulic Research*, 52(1), pp. 105–120. doi: 10.1080/00221686.2014.880859.
Watts, R. J. and Johnson, M. S. (2004) 'Estuaries, lagoons and enclosed embayments: Habitats that enhance population subdivision of inshore fishes', *Marine and Freshwater Research*, 55(7), pp. 641–651. doi: 10.1071/MF04051.
Xiang, K., Yang, Z., Huai, W. and Ding, R. (2019) 'Large eddy simulation of turbulent flow structure in a rectangular embayment zone with different population densities of vegetation', *Environmental Science and Pollution Research*, 26(14), pp. 14583–14597. doi: 10.1007/s11356-019-04709-x.

